Reduced Autophagy in Aged Trigeminal Neurons Causes Amyloid β Diffusion

R. Sonoda[1, 2], E. Kuramoto[2], S. Minami[1, 2], S-E. Matsumoto[3], Y. Ohyagi[4], T. Saito[5], T. Saido[6], K. Noguchi[1], and T. Goto[2]

[1]Department of Periodontology, Graduate School of Medical and Dental Sciences, Kagoshima University, Kagoshima, Japan.

[2]Department of Oral Anatomy and Cell Biology, Graduate School of Medical and Dental Sciences, Kagoshima University, Kagoshima, Japan.

[3]Department of Immunology, Graduate School of Medical and Dental Sciences, Kagoshima University, Kagoshima, Japan.

[4]Department of Neurology and Geriatric Medicine, Ehime University Graduate School of Medicine, Ehime, Japan.

[5]Department of Neurocognitive Science, Institute of Brain Science, Nagoya City University Graduate School of Medical Sciences, Nagoya, Japan.

[6]Laboratory for Proteolytic Neuroscience, RIKEN Center for Brain Science, Wako, Japan.

Abstract word count: 262

Total word count (excluding abstracts, acknowledgments): 3190

Total number of figures: 5 Figurers, 4 Appendix Figures.

Number of references: 33

Keywords: Aging, trigeminal nuclei, autophagosome, beta amyloid, homeostasis, Alzheimer's disease

Abstract

The relationship between oral health and the development of Alzheimer's disease (AD) in the elderly is not yet well understood. In this regard, the association between aging or neurodegeneration of the trigeminal nervous system and the accumulation of amyloid-β Aβ(1-42) $(Aβ)_{42}$ oligomers in the pathogenesis of Alzheimer's disease (AD) is unknown. We focused on selective autophagy in the trigeminal mesencephalic nucleus (Vmes) and the diffusion of $Aβ_{42}$ oligomers with respect to aging of the trigeminal nervous system, and whether the degeneration of Vmes neurons affects the diffusion of $Aβ_{42}$ oligomers. We used female 2–8-month-old transgenic 3×Tg-AD mice and App^{NL-G-F} knock-in mice, and immunohistochemically examined aging-related changes in selective autophagy and $Aβ_{42}$ oligomer processing in the trigeminal mesencephalic nucleus (Vmes), which exhibits high Aβ expression. We induced degeneration of Vmes neurons by extracting the maxillary molars and examined the changes in $Aβ_{42}$ oligomer kinetics. Autophagosome-like membranes, which stained positive for Aβ, HO-1, and LC3B, were observed in Vmes neurons of 3×Tg-AD mice, while there was weak immunoreactivity of the membranes for intra-neuronal Aβ in App^{NL-G-F} mice. By contrast, there was strong immunopositivity for extracellular $Aβ_{42}$ oligomers with the formation of $Aβ_{42}$ oligomer clusters in App^{NL-G-F} mice. The expression of Rubicon, which indicates age-related deterioration of autophagy, increased with the age of Vmes neurons. Tooth extraction increased the extracellular immunopositivity for $Aβ_{42}$ oligomers in App^{NL-G-F} mice. These results suggest that autophagy maintains homeostasis in Vmes neurons, and that deterioration of autophagy due to aging or

neurodegeneration leads to the diffusion of $A\beta_{42}$ oligomers into the extracellular space and possibly the development of AD.

A supplemental appendix to this article is available online.

Corresponding Author:

T. Goto, Department of Oral Anatomy and Cell Biology, Graduate School of Medical and Dental Sciences, Kagoshima University, 35-1 Sakuragaoka, Kagoshima 890-8544, Japan

Email: tgoto@dent.kagoshima-u.ac.jp

Introduction

Alzheimer's disease (AD) is the most common type of dementia. Histopathologically, it is characterized by amyloid-β (Aβ)-containing senile plaques and the accumulation of phosphorylated tau in neurons. AD can be familial or sporadic. Familial AD is associated with mutations of genes such as amyloid precursor protein (APP), presenilin 1, and presenilin 2. AD is typically sporadic or inherited in a non-Mendelian manner; < 1% of cases are inherited in an autosomal dominant manner (Lista et al., 2015; Escamilla-Ayala et al., 2020). The strongest risk factor for AD is advanced age (Scheltens et al., 2016); however, the correlation between neuronal aging and amyloid beta (Aβ) expression, particularly the highly cytotoxic $A\beta_{42}$ oligomer (Jeong et al., 2013), is not clear in AD.

Because of the long life of neurons, neuronal autophagy is thought to be associated with neuronal aging (Stavoe and Holzbaur, 2019). In particular, Rubicon, a molecule that increases with aging, inhibits autophagy (Tanaka et al., 2016). Recent studies have shown that autophagy is important for neuronal homeostasis, particularly mitophagy, which is required for mitochondrial function (Lou et al., 2020). Mitophagy is involved in the function of mitochondria located in the neuronal cell body, as well as in the renewal of mitochondria located at axon terminals (Rappe and McWillams, 2022). Additionally, Aβ and tau are involved in the transport from axon terminals to cell bodies, where autophagy is processed (Stavoe and Holzbaur, 2019). Inside the cell, Aβ is processed by selective autophagy, similar to mitophagy; however, with aging, Aβ is not completely removed by autophagy and is released outside the cell (Menzies et al., 2017; Reddy and Oliver, 2019).

Periodontal disease and the number of remaining teeth have been reported as risk factors for cognitive decline (Takeuchi et al, 2017; Kato et al, 2019; Yoo et al., 2019). We previously used 3×Tg-AD model mice to investigate the role of tooth loss-induced neurodegeneration in the development of AD (Goto et al., 2020), and found the extracellular diffusion of $A\beta_{42}$ occurred after the death of $A\beta_{42}$-IR trigeminal mesencephalic nucleus (Vmes) neuron. Tooth loss is followed by a neurodegenerative cascade in the Vmes, locus coeruleus, and hippocampus, which accelerates the development of AD. Therefore, we have focused on Vmes in examining the relationship between oral health and dementia, including in this study. However, it is unclear how interrelations among neural senescence, autophagy, Aβ diffusion, and neurodegeneration affect the development of AD.

In the present study, we used transgenic 3×Tg-AD mice, which overexpress Aβ, and $App^{NL\text{-}G\text{-}F}$ knock-in mice, which produce Aβ-containing amyloid plaques early in life, to evaluate neuronal autophagy, the dynamics of Aβ, and the role of trigeminal nerve neurodegeneration in the diffusion of $A\beta_{42}$ oligomers.

Materials and Methods

Animals

In this study, we used female transgenic 3×Tg-AD mice and $App^{NL\text{-}G\text{-}F}$ knock-in mice. The 3×Tg-AD mice (back crossed with C57BL/6J mice more than 7 times) are widely used transgenic mice with three mutations (human APP_{swe}, human tau^{P301L}, and human $PS1^{M146V}$) associated with familial AD (Oddo et al., 2003). These mice exhibit both

plaque and tangle pathology. The female *App*$^{NL-G-F}$ mice has a humanized Aβ region that contains the Swedish (*NL*), Iberian (F), and Arctic (G) *App* loci (Saito et al., 2014; Sakakibara et al., 2019). Food and water were provided ad libitum, and animals were maintained on a 12-h light/dark cycle. We used 2-, 3-, 4-, and 8-month-old 3×Tg-AD (n = 27) and *App*$^{NL-G-F}$ (n = 20) mice in total. Non-AD mice, C57BL/6 mice (n=12) with equal genetic background were used. The experiments were approved by the Committee for Animal Experiments of Kagoshima University (approval no.: D17016, D20007). This study conformed to the ARRIVE Guidelines.

Details of the experimental design are described in Appendix 1.

Surgery

Details are given in the Appendix Fig.1.

Immunohistochemistry

Mice (3×Tg-AD mice, n = 21; *App*$^{NL-G-F}$ mice, n = 12; tooth extracted *App*$^{NL-G-F}$ mice, n = 6, C57BL/6, n = 12) were deeply anesthetized using sodium pentobarbital (75 mg/kg) and transcardially perfused with 10 mL of 10 mM phosphate-buffered saline (PBS; pH 7.4) followed by 100 mL of 3% formaldehyde, and 75% saturated picric acid in 0.1 M sodium phosphate (pH 7.0). After cryoprotection with 30% sucrose in PBS, the brainstem containing the Vmes was cut frontally into 50-μm-thick sections using a cryostat. The sections were stored at 4℃ in PBS.

In the following processes for immunoperoxidase staining, sections were incubated at 24℃, and the incubation was followed by rinsing with PBS containing 0.3% Triton

X-100 (PBS-X). The sections were soaked for 30 min in 1% H_2O_2 in PBS, and then incubated overnight with mouse anti-β-amyloid (1–16) antibody (1:1,000; 6E10; BioLegend), and biotinylated donkey anti-mouse IgG antibody (1:200; EMD Millipore) in PBS-X containing 0.12% lambda-carrageenan, and 1% normal donkey serum (Abcam) (PBS-XCD) for 3 h. Then, the sections were incubated with avidin-biotinylated-peroxidase complex (1:100; ABC-Elite; Vector Laboratories) in PBS-X for 1 h. Finally, the sections were incubated with 0.02% diaminobenzidine-4HCl (DAB) and 0.005% H_2O_2 in 50 mM Tris-HCl (pH 7.6) for 10 min. The sections were observed and photographed under an Olympus BX51 microscope and a DP25 camera (Olympus) with cellSens software (Olympus).

For immunofluorescence staining, the following primary antibodies were used: mouse anti-β-amyloid (1–16) (1:1,000; 6E10), rabbit anti-β Amyloid (1-42)-Conformation Specific (1:1,000; GeneTex), rabbit anti-heme oxygenase-1/HMOX1/HSP32 (1:200; Novus Biologicals), rabbit anti-LC3B (1:400; Abcam), and rabbit anti-Rubicon (1:400; Abcam). The sections were incubated overnight with the primary antibodies in PBS-XCD, and subsequently for 4 h with Alexa Fluor 488-, 555- or 647-conjugated donkey anti-mouse or anti-rabbit antibody (1:200; Abcam) in PBS-XCD. Neurons were detected using NeuroTrace green (1:200; ThermoFisher Scientific). All the above incubations were performed at 4°C and followed by rinsing with PBS-X. The sections were imaged under a confocal laser scanning microscope (LSM900; Zeiss). Negative controls for immunostaining were performed using the same immunostaining method, only excluding the primary antibody. The data analysis was performed by experimenters who were blinded to the mice strain, age, and conditions. Analysis of immunostaining are described in the Appendix Figure 2.

Immunoelectron microscopy

For immunoelectron microscopy, 4-month-old 3×Tg-AD mice (n = 2) were deeply anesthetized and perfused transcardially with 10 mL of PBS, and followed by 200 mL of 0.05% glutaraldehyde and 4% paraformaldehyde in 0.1 M sodium phosphate buffer (PB; pH 7.4). After postfixation with 4% paraformaldehyde in 0.1 M PB for 4 h, the brain blocks were cut into 50-μm-thick sections using a vibratome. To suppress endogenous peroxidase, the sections were incubated with 1% H_2O_2 in PBS for 30 min, and then preincubated with PBS containing 20% normal donkey serum for 1 h to block nonspecific antibody binding. The following incubations were performed at 4°C in PBS containing 10% normal donkey serum and 0.2% Photoflo (Fujifilm). The sections were incubated with mouse anti-β-amyloid (1–16) antibody (1:1,000) overnight. Then, the sections were incubated with biotinylated donkey anti-mouse IgG (1:100) for 4 h, followed by incubation with ABC-Elite (1:50) for 4 h. The bound ABC in the sections was developed in brown for 20–40 min in a DAB reaction mixture containing 0.02% DAB and 0.001% H_2O_2 in 50 mM Tris-HCl (pH 7.6). The sections were postfixed with 1% osmium tetroxide in 0.1 M PB, stained with 1% uranyl acetate in distilled water, dehydrated using an ethanol series, and embedded flat in an epoxy resin (Luvek 812). After polymerization of the resin, the tissue samples were cut into ultrathin sections (70 nm) using an ultramicrotome. Ultrathin sections were mounted on grids and observed using an electron microscope H7650 (Hitachi).

Statistical analysis

Numbers and error bars represent means ± standard deviations. Images were analyzed using ImageJ software (NIH). Means were compared using unpaired Student's *t*-test or one-way analysis of variance followed by Tukey's *post-hoc* test, performed using R Software (R Foundation for Statistical Computing).

Results

Distribution of Aβ in Vmes neurons of 3×Tg-AD mice

Vmes neurons of 4-month-old 3×Tg-AD mice showed strongly positive staining with anti-Aβ antibody (6E10) (Fig. 1A). No immunopositivity was found in negative controls (Appendix Fig. 3). To determine the localization of Aβ in Vmes neurons, immunofluorescent staining was performed (Fig. 1B). Observation of the stained sections at high magnification using a laser scanning microscope revealed numerous membrane-like structures within the cells (Fig. 1C). Visualization under higher magnification confirmed the localization of Aβ in axons of Vmes neurons (Fig. 1D and E).

Immunoelectron microscopy was used to examine the intracellular localization of Aβ, which showed strong Aβ immunopositivity in the short membranous structures (Fig. 1F and G). The enlarged circular membrane showed strong Aβ immunopositivity on the outer surface of the membrane (Fig. 1H and I), and structures with an appearance similar to mitochondria were found inside the membrane. The Aβ immunopositivity and

presence of mitochondria surrounded by membrane suggest that these Aβ-immunoreactive (IR) membranes are autophagic.

Autophagy in Vmes neurons of 3×Tg-AD mice

The Aβ-IR membrane within Vmes neurons of 4-month-old 3×Tg-AD mice showed the morphological characteristics of autophagy-related membranes (Fig. 2A). To investigate the characteristics of this autophagy-related membrane-like structure, we double-stained the sections using anti-HO-1 (a marker of endoplasmic reticulum, ER) and anti-Aβ antibodies (Fig. 2B). Three forms of Aβ-IR/HO-1-IR membrane were observed.: Crescent-shaped (Fig. 2C), unclosed circular (Fig. 2D), and closed circular Aβ-IR/HO-1-IR membrane (Fig. 2E).

Both Aβ-IR and HO-1-IR membranes were structurally similar to autophagy-associated membranes (i.e., the crescent-shaped membrane is the ER membrane, the non-closed circular membrane is the phagophore, and the closed circular membrane is the autophagosome) (Fig. 2F). To investigate age-related changes in autophagy in neurons, we examined changes in the ratio of these membrane types with cell aging. The ER membrane was the most abundant membrane type in Vmes neurons of all ages, followed by phagophore and autophagosome; however, there was no significant difference in the ratio of the three membranes according to neuronal age (Fig. 2G).

Next, to determine whether these membranes were associated with autophagy, we examined the coexistence of Aβ and LC3B, which are markers of autophagy-associated membranes (Kabeya et al., 2000). Among Vmes neurons, some had stronger Aβ-IR, whereas others had stronger LC3B-IR. Additionally, the strength of Aβ-IR varied

among Vmes neurons (Fig. 2H). Double immunostaining for Aβ and LC3B showed that LC3B was present and in contact with Aβ-IR, although few areas were completely double-stained (Fig. 2I–L). Some Vmes neurons with greater LC3B-IR than Aβ-IR were also observed (Fig. 2M). These findings suggest that not all autophagic membranes of Vmes neurons expressed Aβ.

Intracellular and extracellular distribution of $A\beta_{42}$ oligomer in 3×Tg-AD and App^{NL-G-F} mice

Of the various Aβ types, $A\beta_{42}$ oligomer has most recently been implicated in AD progression. Because 3×Tg-AD mice overexpress Aβ, we compared the intracellular and extracellular expression levels of $A\beta_{42}$ oligomer in 3×Tg-AD and App^{NL-G-F} knock-in mice, which do not overexpress Aβ. Staining of Vmes neurons with anti-$A\beta_{42}$ oligomer antibody revealed stronger intracellular immunopositivity in App^{NL-G-F} than 3×Tg-AD mice (Fig. 3A–J). Extracellular $A\beta_{42}$ oligomer immunopositivity was rarely observed in 3×Tg-AD mice, whereas $A\beta_{42}$ oligomer clusters were observed in App^{NL-G-F} mice (Fig. 3K–T). Intracellular and extracellular $A\beta_{42}$ oligomer immunopositivity was significantly greater in App^{NL-G-F} compared to 3×Tg-AD mice (Fig. 3U and V). Since extracellular $A\beta_{42}$ oligomers were identified in App^{NL-G-F} mice, App^{NL-G-F} mice were used in this later experiment.

Age-related Rubicon appearance in Vmes neurons of App^{NL-G-F} and C57BL/6 mice.

Diffusion of $A\beta_{42}$ oligomers outside the cell may be caused by an aging-related reduction in cellular autophagy. Rubicon is an autophagy-related molecule and inhibitor of autophagy associated with cellular senescence. We examined the expression of Rubicon in Vmes neurons of aged 2-, 3-, and 4-month-old $App^{NL\text{-}G\text{-}F}$ and C57BL/6 mice. We found that both groups had fewer Rubicon immunopositivity at 2 months of age; at 3 and 4 months of age, both groups had increased Rubicon immunopositivity in Vmes neurons (A). Interestingly, both groups showed a wide range of strong immunopositivity for Rubicon around neurons. Quantitative analysis revealed significantly ($p < 0.0001$) more intracellular immunopositivity for Rubicon in neurons from 3- to 4-month-old $App^{NL\text{-}G\text{-}F}$ mice than wild-type C57BL/6 mice. Similar findings to those in $App^{NL\text{-}G\text{-}F}$ mice were observed in 3×Tg-AD mice (Appendix Fig. 4).

Extracellular distribution of $A\beta_{42}$ oligomers after tooth extraction

In addition to cellular aging, tooth extraction is a predisposing factor for Vmes neuronal degeneration. We evaluated whether the level of extracellular $A\beta_{42}$ oligomers was increased after tooth extraction. $App^{NL\text{-}G\text{-}F}$ mice underwent extraction of a right maxillary molar at 2.5 months of age. Two weeks after the extraction, Aβ42 oligomer immunopositivity in the vicinity of the right Vmes cells was examined. As a control, Aβ42 oligomer immunopositivity in the vicinity of Vmes cells on the left side where no tooth extraction was performed was examined.

In 3-month-old $App^{NL\text{-}G\text{-}F}$ mice without tooth extraction, Vmes neurons had a relatively large, circular morphology and few extracellular $A\beta_{42}$ oligomers (Fig. 5A–C).

Two weeks after tooth extraction, some Vmes neurons showed morphological changes and clusters of $A\beta_{42}$ oligomer immunopositivity near the neurons (Fig. 5D–F). Quantitative analysis of extracellular $A\beta_{42}$ oligomers showed significantly more extracellular $A\beta_{42}$ oligomers in $App^{NL\text{-}G\text{-}F}$ mice 2 weeks after tooth extraction than in mice without tooth extraction (Fig. 5G).

Discussion

Vmes neurons in 3xTg-AD mice exhibited prominent Aβ expression; additionally, immunoelectron microscopy revealed Aβ immunopositivity on membranes that appeared similar to autophagy membranes, and mitochondria were observed within these autophagosome-like structures. High-magnification immunofluorescence staining revealed Aβ-IRs on axons of Vmes neurons, suggesting that Aβ is involved in axonal transport. The 3×Tg-AD mouse is an early-generation transgenic model mouse of AD that exhibits Aβ expression and cognitive dysfunction (Crews et al., 2010). Since in transgenic mice, but not knock-in mice, the transgene is inserted randomly, which has been shown to disrupt unexpectedly large regions of the host animal's endogenous locus (Gamache et al., 2019), which may associate with the fact that the 3xTg-AD mice over expressed levels of Aβ, and Aβ overexpression is a major limitation of this AD mouse model. Therefore, we also used $App^{NL\text{-}G\text{-}F}$ mice which do not overexpress Aβ. Interestingly, the $App^{NL\text{-}G\text{-}F}$ mice, which expressed less intracellular Aβ, showed more immunopositive responses for $A\beta_{42}$ oligomers than 3×Tg-AD, and $A\beta_{42}$ oligomers were also observed extracellularly, which were not observed in the 3×Tg-AD mice. Although previous studies have shown that extracellular release of Aβ is caused by APP cleavage

at the plasma membrane (Chyung et al., 2005), we did not observe Aβ-IR on the plasma membrane in the present study; however, Aβ-IR was observed on the intracellular HO-1-IR ER membrane. It is likely that the Aβ generated by APP cleavage on the intracellular membrane is mostly returned to the soma by axonal transport for degradation or reuse by autophagy. Furthermore, some Aβ are also produced intracellularly as $A\beta_{42}$ oligomers, which may be processed by autophagy or released extracellularly.

To determine whether the Aβ-IR membrane is an autophagy-related membrane, we examined the localization of HO-1, a marker of the autophagy-related ER membrane (Zhao et al., 2013), and LC3B, an autophagy-related molecule (Wu et al., 2006), and found immunopositivity for HO-1 and LC3B in the Aβ-IR membrane. However, we also found certain LC3B molecules that did not coexist with the Aβ-IR membrane, suggesting that Aβ is not found on all autophagy-related membranes. If Aβ-IR membranes are autophagy-related, there should be three morphological types thereof: ER membranes, phagophores, and autophagosomes (Burman and Ktistakis, 2010). Indeed, three types of Aβ-IR membranes were identified in the present study. The intracellular proportions of these membranes were similar in Vmes neurons of 2-, 4-, and 8-month-old mice, suggesting that the formation of autophagy-related membranes, which maintains neuronal homeostasis, persists even in aged neurons.

Previously, $A\beta_{42}$ [amyloid β peptide-(1–42)] was considered the most toxic type of Aβ in AD (Wilson et al., 1999). However, recently, soluble $A\beta_{42}$ oligomers have been found to be the most neurotoxic Aβ in AD (Lazzari et al., 2015). Although extracellular $A\beta_{42}$ production has been well-documented (Ma et al., 1994), few studies have evaluated the intracellular production of $A\beta_{42}$ oligomers (Deshpande et al., 2009). In our

study, interestingly, transgenic AD mice with Aβ overexpression had fewer extracellular $A\beta_{42}$ oligomers than APP knock-in mice, whose extracellular $A\beta_{42}$ oligomers formed clusters. *App*$^{NL\text{-}G\text{-}F}$ mice formed amyloid plaques at the age of 2 months, while 3×Tg-AD mice require > 6 months to form amyloid plaques (Sasaguri et al., 2022). Our results indicate that *App*$^{NL\text{-}G\text{-}F}$ mice are more useful than 3×Tg-AD mice for studying the behavior of intracellular and extracellular $A\beta_{42}$ oligomers in neurons. In addition, regarding 3×Tg-AD mice, it has been reported that "male 3×Tg-AD mice may not exhibit the phenotype initially described" (jax.org, B6; 129-Tg(APPSwe,tauP301L)1Lfa Psen1^{tm1Mpm}/Mmjax), we have unified the sex of the mice to females in this experiment.

To investigate the relationship between neuronal aging and $A\beta_{42}$ oligomers, we focused on neuronal autophagy. We hypothesized that neuronal aging might be associated with the excretion of undigested $A\beta_{42}$ oligomers from cells. Rubicon is a molecule implicated in the age-related decline of autophagy in neurons, and its expression increases with cellular age. It interferes with the fusion of autophagosomes and lysosomes, and inhibits autophagy (Tabata et al., 2010, Nakamura et al., 2019). In the *App*$^{NL\text{-}G\text{-}F}$ mice in this study, Rubicon expression increased with aging in Vmes neurons, and there were significantly more Rubicon-immunoreactivity in neurons from 3- and 4-month-old *App*$^{NL\text{-}G\text{-}F}$ mice compared to wild-type C57BL/6 mice of same age. This means that as cells age in AD model mice, some molecules such as Rubicon inhibit autophagy, resulting in the release and diffusion of undigested $A\beta_{42}$ oligomers to the extracellular space. Soluble $A\beta_{42}$ oligomers are cytotoxic to the surrounding cells and form clusters, leading to the formation of amyloid plaques. However, since mice and humans have different life spans, a limitation of this study is whether the increase in

Rubicon in cells observed in 3- and 4-month-old mice replicates neural senescence in humans. Further studies are needed to determine whether the expression of Rubicon in neurons, i.e., deteriorated autophagy, correlates with the progress of AD in the human brain.

Finally, we examined the effects of tooth extraction on the neurodegeneration and diffusion of $A\beta_{42}$ oligomers in $App^{NL\text{-}G\text{-}F}$ mice. Vmes neurons with damaged nerve endings due to tooth extraction showed morphological changes and significantly increased extracellular $A\beta_{42}$ oligomer levels compared to the normal Vmes neurons. Tooth extraction induced neurodegeneration in Vmes neurons (Dhar et al., 2021); this may have suppressed neuronal autophagy, resulting in the diffusion of large quantities of undigested $A\beta_{42}$ oligomers. Previous studies of 3×Tg-AD mice showed that tooth extraction triggers the onset of AD through a neurodegenerative cascade in the Vmes-locus coeruleus-hippocampus pathway. Furthermore, in the present experiments on $App^{NL\text{-}G\text{-}F}$ mice, many $A\beta_{42}$ oligomers diffused extracellularly. Therefore, tooth extraction during the period of cognitive decline in patients with genetic mutations related to AD would indicate a potential risk for disease progression.

In summary, the present study demonstrated increased Rubicon expression in Vmes neurons with aging especially in AD model mice. Rubicon inhibits autophagy in neurons and promotes the diffusion of partially degraded $A\beta_{42}$ oligomers outside of neurons. The extracellular diffusion of $A\beta_{42}$ oligomers was greater in knock-in than in transgenic AD model mice. Our results suggest that autophagy maintains homeostasis in Vmes neurons, and that age-related deterioration of autophagy and neurodegeneration promote the diffusion of $A\beta_{42}$ oligomers to the extracellular space, leading to the development of AD.

Author Contribution

R. Sonoda, contributed to conception, design, immune-staining and observation, statistical analysis, drafted and critically revised the manuscript. E. Kuramoto, contributed to conception, design, immunoelectron-staining, and observation, drafted, and critically revised the manuscript. S. Minami contributed to conception, design, immunoelectron-staining, and observation. S. Matsumoto, contributed to conception, design, critically revised the manuscript. Y. Ohyagi provided 3×Tg-AD mice, contributed to conception, design, critically revised the manuscript. T. Saito and T Saido provided $App^{NL\text{-}G\text{-}F}$ mice, and contributed to conception, design, critically revised the manuscript. K. Noguchi contributed to conception, and critically revised the manuscript. T. Goto contributed to conception, design, observation, drafted and critically revised the manuscript. All authors contributed to the article and approved the submitted version.

Acknowledgments

We would like to thank Dr. Frank LaFerla (University of California, Irvine) for originally providing breeding pairs of 3×Tg-AD mice to Dr. Y. Ohyagi who is a coauthor of the manuscript.

Declaration of Conflicting Interest

The authors declared no conflict of interest with respect to the research, authorship, and publication of this article.

Funding

This research was supported by a Grant-in-Aid for Scientific Research (C) (19K10058, 22K09916 to Kuramoto, 20K10296 to Goto), for Challenging Exploratory Research (22K19636 to Goto), and for Scientific Research on Innovative Areas (17H06311, 22H05162 to Kuramoto) from the Ministry of Education, Culture, Sports, Science and Technology, Japan.

ORCID iDs

E Kuramoto https://orcid.org/0000-0002-0636-541X

S-E Matsumoto https://orcid.org/0000-0002-4283-202X

T Saito https://orcid.org/0000-0002-9659-9251

T Saido https://orcid.org/0000-0003-1970-6903

K Noguchi https://orcid.org/0000-0003-4327-1698

T Goto https://orcid.org/0000-0002-9935-8971

References

Burman C, Ktistakis NT. 2010. Autophagosome formation in mammalian cells. Semin Immunopathol. 32(4):397-413.

Chyung JH, Raper DM, Selkoe DJ. 2005. Gamma-secretase exists on the plasma membrane as an intact complex that accepts substrates and effects intramembrane cleavage. J Biol Chem. 280(6):4383-92.

Crews L, Rockenstein E, Masliah E. 2010. APP transgenic modeling of Alzheimer's disease: mechanisms of neurodegeneration and aberrant neurogenesis. Brain Struct Funct. 214(2):111-126.

Deshpande A, Kawai H, Metherate R, Glabe CG, Busciglio J. 2009. A role for synaptic zinc in activity-dependent Abeta oligomer formation and accumulation at excitatory synapses. J Neurosci. 29(13):4004-4015.

Dhar A, Kuramoto E, Fukushima M, Iwai H, Yamanaka A, Goto T. 2021. The Periodontium Damage Induces Neuronal Cell Death in the Trigeminal Mesencephalic Nucleus and Neurodegeneration in the Trigeminal Motor Nucleus in C57BL/6J Mice. Acta Histochem Cytochem. 54(1): 11-19.

Escamilla-Ayala A, Wouters R, Sannerud R, Annaert W. 2020. Contribution of the Presenilins in the cell biology, structure and function of γ-secretase. Semin Cell Dev Biol. Sep;105:12-26.

Gamache J, Benzow K, Forster C, Kemper L, Hlynialuk C, Furrow E, Ashe KH, Koob MD. 2019. Factors other than hTau overexpression that contribute to tauopathy-like phenotype in rTg4510 mice. Nat Commun. 10(1):2479.

Goto T, Kuramoto E, Dhar A, Wang RP, Seki H, Iwai H, Yamanaka A, Matsumoto SE, Hara H, Michikawa M, Ohyagi Y, Leung WK, Chang RC. 2020.

Neurodegeneration of trigeminal mesencephalic neurons by the tooth loss triggers the progression of Alzheimer's disease in 3×Tg-AD model mice. J Alzheimers Dis. 76(4):1443-1459.

Jeong JS, Ansaloni A, Mezzenga R, Lashuel HA, Dietler G. 2013. Novel mechanistic insight into the molecular basis of amyloid polymorphism and secondary nucleation during amyloid formation. J Mol Biol. 425(10):1765-1781.

Kabeya Y, Mizushima N, Ueno T, Yamamoto A, Kirisako T, Noda T, Kominami E, Ohsumi Y, Yoshimori T. 2000. LC3, a mammalian homologue of yeast Apg8p, is localized in autophagosome membranes after processing. EMBO J. 19(21):5720-5728.

Kato H, Takahashi Y, Iseki C, Igari R, Sato H, Sato H, Koyama S, Tobita M, Kawanami T, Iino M, Ishizawa K, Kato T. 2019. Tooth Loss-associated Cognitive Impairment in the Elderly: A Community-based Study in Japan. Intern Med. 58(10): 1411-1416.

Lazzari C, Kipanyula MJ, Agostini M, Pozzan T, Fasolato C. 2015. Aβ42 oligomers selectively disrupt neuronal calcium release. Neurobiol Aging. 36(2):877-885.

Lista S, O'Bryant SE, Blennow K, Dubois B, Hugon J, Zetterberg H, Hampel H. 2015. Biomarkers in sporadic and familial Alzheimer's disease. J Alzheimers Dis. 47(2):291-317.

Lou G, Palikaras K, Lautrup S, Scheibye-Knudsen M, Tavernarakis N, Fang EF. 2020. Mitophagy and Neuroprotection. Trends Mol Med. 26(1):8-20.

Ma J, Yee A, Brewer HB Jr, Das S, Potter H. 1994. Amyloid-associated proteins alpha 1-antichymotrypsin and apolipoprotein E promote assembly of Alzheimer beta-protein into filaments. Nature. 372(6501):92-94.

Menzies FM, Fleming A, Caricasole A, Bento CF, Andrews SP, Ashkenazi A, Füllgrabe J, Jackson A, Jimenez Sanchez M, Karabiyik C, Licitra F, Lopez Ramirez A, Pavel M, Puri C, Renna M, Ricketts T, Schlotawa L, Vicinanza M, Won H, Zhu Y, Skidmore J, Rubinsztein DC. 2017. Autophagy and neurodegeneration: pathogenic mechanisms and therapeutic opportunities. Neuron. 93(5):1015-1034.

Nakamura S, Oba M, Suzuki M, Takahashi A, Yamamuro T, Fujiwara M, Ikenaka K, Minami S, Tabata N, Yamamoto K, Kubo S, Tokumura A, Akamatsu K, Miyazaki Y, Kawabata T, Hamasaki M, Fukui K, Sango K, Watanabe Y, Takabatake Y, Kitajima TS, Okada Y, Mochizuki H, Isaka Y, Antebi A, Yoshimori T. 2019. Suppression of autophagic activity by Rubicon is a signature of aging. Nat Commun. 10(1):847.

Oddo S, Caccamo A, Shepherd JD, Murphy MP, Golde TE, Kayed R, Metherate R, Mattson MP, Akbari Y, LaFerla FM. 2003. Triple-transgenic model of Alzheimer's disease with plaques and tangles: intracellular Abeta and synaptic dysfunction. Neuron. 39(3):409-421.

Rappe A, McWilliams TG. 2022. Mitophagy in the aging nervous system. Front Cell Dev Biol. 10:978142.

Reddy PH, Oliver DM. 2019. Amyloid beta and phosphorylated tau-induced defective autophagy and mitophagy in Alzheimer's disease. Cells. 8(5):488.

Saito T, Matsuba Y, Mihira N, Takano J, Nilsson P, Itohara S, Iwata N, Saido TC. 2014. Single App knock-in mouse models of Alzheimer's disease. Nat Neurosci. 17(5):661-663.

Sakakibara Y, Sekiya M, Saito T, Saido TC, Iijima KM. 2019. Amyloid-β plaque formation and reactive gliosis are required for induction of cognitive deficits in App knock-in mouse models of Alzheimer's disease. BMC Neurosci. 20(1):13.

Sasaguri H, Hashimoto S, Watamura N, Sato K, Takamura R, Nagata K, Tsubuki S, Ohshima T, Yoshiki A, Sato K, Kumita W, Sasaki E, Kitazume S, Nilsson P, Winblad B, Saito T, Iwata N, Saido TC. 2022. Recent advances in the modeling of Alzheimer's disease. Front Neurosci. 16:807473.

Scheltens P, Blennow K, Breteler MM, de Strooper B, Frisoni GB, Salloway S, Van der Flier WM. 2016. Alzheimer's disease. Lancet. 388(10043):505-17.

Stavoe AKH, Holzbaur ELF. 2019. Autophagy in neurons. Annu Rev Cell Dev Biol. 35:477-500.

Tabata K, Matsunaga K, Sakane A, Sasaki T, Noda T, Yoshimori T. 2010. Rubicon and PLEKHM1 negatively regulate the endocytic/autophagic pathway via a novel Rab7-binding domain. Mol Biol Cell. 21(23):4162-4172.

Takeuchi K, Ohara T, Furuta M, Takeshita T, Shibata Y, Hata J, Yoshida D, Yamashita Y, Ninomiya T. 2017. Tooth Loss and Risk of Dementia in the Community: the Hisayama Study. J Am Geriatr Soc. 65:e95-e100.

Tanaka S, Hikita H, Tatsumi T, Sakamori R, Nozaki Y, Sakane S, Shiode Y, Nakabori T, Saito Y, Hiramatsu N, Tabata K, Kawabata T, Hamasaki M, Eguchi H, Nagano H, Yoshimori T, Takehara T. 2016. Rubicon inhibits autophagy and accelerates hepatocyte apoptosis and lipid accumulation in nonalcoholic fatty liver disease in mice. Hepatology. 64(6):1994-2014.

Wilson CA, Doms RW, Lee VM. 1999. Intracellular APP processing and A beta production in Alzheimer disease. J Neuropathol Exp Neurol. 58(8):787-794.

Wu J, Dang Y, Su W, Liu C, Ma H, Shan Y, Pei Y, Wan B, Guo J, Yu L. 2006. Molecular cloning and characterization of rat LC3A and LC3B--two novel markers of autophagosome. Biochem Biophys Res Commun. 339(1):437-42.

Yang AJ, Chandswangbhuvana D, Shu T, Henschen A, Glabe CG. 1999. Intracellular accumulation of insoluble, newly synthesized abetan-42 in amyloid precursor protein-transfected cells that have been treated with Abeta1-42. J Biol Chem. 274(29):20650-20656.

Yoo JJ, Yoon JH, Kang MJ, Kim M, Oh N. 2019. The effect of missing teeth on dementia in older people: a nationwide population-based cohort study in South Korea. BMC Oral Health. 19(1): 61.

Zhang X, Zhang L, Li J, Wang W, Zhou L, Gao X. 2013. Heme oxygenase-1 prevents cardiac dysfunction in streptozotocin-diabetic mice by reducing inflammation, oxidative stress, apoptosis and enhancing autophagy. PLoS One. 8(9):e75927.

Figure Legends

Figure 1. Distribution of Aβ in the trigeminal mesencephalic nucleus in 4-month-old 3×Tg-AD mice evaluated using anti-Aβ antibody (6E10). Aβ-IR Vmes neurons at low magnification evaluated using immunoperoxidase staining (**A**) and immunofluorescence (Alexa Fluor 555; excitation, 543 nm; emission, 590–625 nm) (**B**). (**C**) Higher magnification image of the cell body of an Aβ-IR Vmes neuron. Immunofluorescence images of Aβ-IR neurons (**D**). Aβ-IR axon (arrow) of a Vmes neuron (rectangle in **D)** **(E)**. Digital images were captured under the confocal laser-scanning microscope (LSM 900; Zeiss), (B) with a 10× objective (Plan-Apochromat, numerical aperture = 0.45; Zeiss), (D) with an oil immersion 63× objective (Plan-Apochromat, numerical aperture = 1.4; Zeiss) and a pinhole 1.0 Airy unit, and (C) and (E) were taken with a zoom factor of 2.4. (**F**) An immunoelectron microscopy image of Aβ-IR membranes. N: nucleus. (**G**) Higher magnification image of the area inside the rectangle in **F**. Strong Aβ immunoreactivity localized on the ER membrane (arrows). (**H**) Aβ-IR phagosome-like structures (arrows) at the peripheral part of Vmes neuron. (**I**) Mitochondria-like structure (arrowhead). Aβ immunoreactivity on the membrane (arrow) and outside the membrane (double arrows). Scale bars = **A** and **B**, 100 μm; **C**–**E**, 10 μm; **F**, 5 μm; **G** and **H**, 2 μm; **I**, 500 nm.

Figure 2. Aβ-related autophagic membranes in Vmes neurons of 3×Tg-AD mice. The sections that contained Vmes neurons were immunostained for Aβ (Alexa Fluor 555; excitation, 543 nm; emission, 590–625 nm), HO-1 and LC3B (Alexa Fluor 647; excitation, 633 nm; emission, ≥ 650 nm). Digital images were captured under the

confocal laser-scanning microscope (LSM 900; Zeiss), (H) with a 20× objective (Plan-Apochromat, numerical aperture = 0.8; Zeiss), (A, C–E, I–M) with an oil immersion 63× objective (Plan-Apochromat, numerical aperture = 1.4; Zeiss) and a pinhole 1.0 Airy unit, with a zoom factor of 1.0–4.8. (**A**, **B**) Immunofluorescence images of Aβ-IR (**A**) and Aβ-IR/HO-1-IR structures in Vmes neurons. (**C**–**E**) Higher magnification images of the colocalization of Aβ and HO-1 immunopositivity within the rectangles **C, D**, and **E** in **B** (arrow: HO-1, arrowhead: Aβ). The shapes of Aβ-IR/HO-1-IR membranes represent the process of macroautophagy; the crescent-shaped Aβ-IR/HO-1-IR membrane is the ER membrane (**C**), the non-closed circular Aβ-IR/HO-1-IR membrane is the phagophore (**D**), and the closed circular Aβ-IR/HO-1-IR membrane is the autophagosome (**E**). (**F**) Schematic of the three macroautophagic membrane types; ER membrane, phagophore, and autophagosome. (**G**) Ratio of ER membranes, **C** type ; phagophores, **D** type; and autophagosomes, **E** type to total Aβ-IR/HO-1-IR membranes per neurons by age (2, 4, and 8 months). For morphological analysis of ER membranes (**G**), digital images were captured under the confocal laser-scanning microscope with an oil immersion 63× objective (Plan-Apochromat, numerical aperture = 1.4; Zeiss) and a pinhole 1.0 Airy unit, with a zoom factor of 4.8. We selected 15 sections, which were spaced at regular intervals within the caudal half part of the Vmes from 9 mice, and captured images of a randomly selected one Vmes neuron per section. Thus, we captured 15-images from 9 mice in total. Data are means ± SDs, n = 5. (**H**) Low magnification immunofluorescence images of Aβ-IR/LC3-IR structures in Vmes neurons. High magnification image of Aβ (**I**) and LC3B (**J**) immunopositivity in a Vmes neuron. (**K**) A merged image of **I** and **J**. (**L**) Co-localization of Aβ (arrowheads) and LC3B (arrows) within the rectangle in **K**. (**M**) Vmes neurons with strong

immunopositivity for LC3B (left) and Aβ/LC3B (right). Scale bars = **A, B**, and **I–K**, 10 μm; **C** and **D**, 1 μm; **E** and **L**, 0.5 μm; H, 50 μm; M, 20 μm.

Figure 3. Differential appearance of the immunopositivity of Aβ and $A\beta_{42}$ oligomers in 4-month-old 3×Tg-AD and $App^{NL\text{-}G\text{-}F}$ mice. The sections that contained Vmes neurons were stained with NeuroTrace Green (NG; excitation 488 nm, emission 505–530 nm) and immunostained for Aβ (Alexa Fluor 555; excitation, 543 nm; emission, 590–625 nm) and Aβ42 oligomers (Alexa Fluor 647; excitation, 633 nm; emission, ≥ 650 nm). Digital images were captured under the confocal laser-scanning microscope (LSM 900; Zeiss), (K–T) with a 10× objective (Plan-Apochromat, numerical aperture = 0.45; Zeiss), (A–J) with an oil immersion 63× objective (Plan-Apochromat, numerical aperture = 1.4; Zeiss) and a pinhole 1.0 Airy unit. High magnification immunofluorescence images of immunopositivity for Aβ and $A\beta_{42}$ oligomers within Vmes neurons of 3×Tg-AD (**A**–**D)** and $App^{NL\text{-}G\text{-}F}$ (**F**–**I**) mice. (**E**, **J**) In the captured images, intracellular $A\beta_{42}$ oligomer-immunopositive areas were binarized (red). Values indicate the percentage of areas immunopositive for $A\beta_{42}$ oligomers within the encircled areas by solid lines (cell bodies). Low magnification immunofluorescence images of Aβ and $A\beta_{42}$ oligomer immunopositivity in 3×Tg-AD (**K–N**) and $App^{NL\text{-}G\text{-}F}$ (**P–S**) mice. (**O**, **T**) In the captured images, extracellular $A\beta_{42}$ oligomer-immunopositive areas were binarized (red). Values indicate the Proportion of extracellular areas immunopositive for $A\beta_{42}$ oligomers (red) within a 640-μm square that excluded Vmes neurons. For quantitative analysis (U, V), we selected 10 sections, which were spaced at regular intervals within the caudal half part of the Vmes from 4 $App^{NL\text{-}G\text{-}F}$ and 3×Tg-AD mice each (20 sections from 8 mice, in total). We captured images of a randomly selected one

Vmes neuron per section using the confocal laser-scanning microscope (LSM 900; Zeiss) with an oil immersion 63× objective (Plan-Apochromat, numerical aperture = 1.4; Zeiss) and a pinhole 1.0 Airy unit for intracellular analysis, and captured the images of a randomly selected the whole Vmes per section with a 10× objective (Plan-Apochromat, numerical aperture = 0.45; Zeiss) for extracellular analysis. Thus, we captured 20-images from 8 mice in total. For more details, see Appendix Figure 2. (**U**) Graph showing the difference in ratio of intracellular immunopositive areas for $A\beta_{42}$ oligomers to the total cell area in Vmes neurons between 3×Tg-AD and $App^{NL\text{-}G\text{-}F}$ mice. Data are presented as means ± SDs, n = 5. ****$p < 0.0001$, unpaired *t*-test. (**V**) Graph showing the difference in ratio of extracellular immunopositive areas for $A\beta_{42}$ oligomers in a 640-μm square between 3×Tg-AD and $App^{NL\text{-}G\text{-}F}$ mice. Data are means ± SDs, n = 5. **$p = 0.009$, unpaired *t*-test. Scale bars = E and J, 10 μm; O and T, 100 μm.

Figure 4. Increased Rubicon expression of aged Vmes neurons in $App^{NL\text{-}G\text{-}F}$ and C57BL/6 mice. (**A**) Vmes neurons from $App^{NL\text{-}G\text{-}F}$ mice (left) and C57BL/6 mice (right) aged 2, 3, and 4 months were immunostained for Rubicon (Alexa Fluor 647; excitation, 633 nm; emission, ≥ 650 nm) and counterstained with NeuroTrace Green (NG; excitation 488 nm, emission 505–530 nm) to visualize neuron shape. For quantitative analysis (G), we selected 15 sections, which were spaced at regular intervals within the caudal half part of the Vmes from 12 $App^{NL\text{-}G\text{-}F}$ and C57BL/6J mice each (30 sections from 24 mice, in total). We captured images of a randomly selected one Vmes neuron per section using the confocal laser-scanning microscope (LSM 900; Zeiss) with an oil immersion 63× objective (Plan-Apochromat, numerical aperture = 1.4; Zeiss) and a pinhole 1.0 Airy unit. (**B**) Graph showing the difference in the ratio of immunopositive

areas for Rubicon to the cell area analyzed in the same way shown in Appendix Figure 2. Scale bars = 10 μm (C, F, I). Data are means ± SDs, n = 5. ****$p < 0.0001$, one-way analysis of variance followed by Tukey's *post-hoc* test.

Figure 5. Neuronal degeneration and $A\beta_{42}$ oligomer diffusion after tooth extraction in $App^{NL\text{-}G\text{-}F}$ mice. Immunofluorescence images of $A\beta_{42}$ oligomer immunopositivity (Alexa Fluor 647; excitation, 633 nm; emission, ≥ 650 nm), (**A**–**C**) in a Vmes neuron on the left side where no tooth extraction was performed, and (**D**–**F**) in a Vmes neuron of $App^{NL\text{-}G\text{-}F}$ mouse two weeks after right-maxillary molars extraction at 2.5 months of age. The sections were counterstained with NeuroTrace Green (NG; excitation 488 nm, emission 505–530 nm) to visualize neuron shape. For quantitative analysis (G), we selected 10 sections, which were spaced at regular intervals within the caudal half part of the Vmes from 6 $App^{NL\text{-}G\text{-}F}$ mice (three tooth extracted mice and three non-extracted mice). We analyzed the caudal half of the Vmes because previous our papers have shown that the caudal half of the Vmes is affected by tooth extraction (Goto et al., 2020; Dhar et al., 2021); Vmes neurons innervate the ipsilateral periodontal ligament and muscle spindles, so we analyzed Vmes neurons on the side ipsilateral to the tooth extraction. We captured images of a randomly selected one Vmes neuron per section using the confocal laser-scanning microscope (LSM 900; Zeiss) with an oil immersion 63× objective (Plan-Apochromat, numerical aperture = 1.4; Zeiss) and a pinhole 1.0 Airy unit. (**G**) Graphs show the ratio of the area of $A\beta_{42}$ oligomer immunopositivity in the extracellular region. Neurons were placed in the center of a 40-μm square, and the ratio of extracellular $A\beta_{42}$ oligomer immunopositive area to the area of the square excluding

the area of the cells was measured. Data are means ± SDs, n = 5. *$p < 0.05$, unpaired t-test. Scale bar = 10 μm.

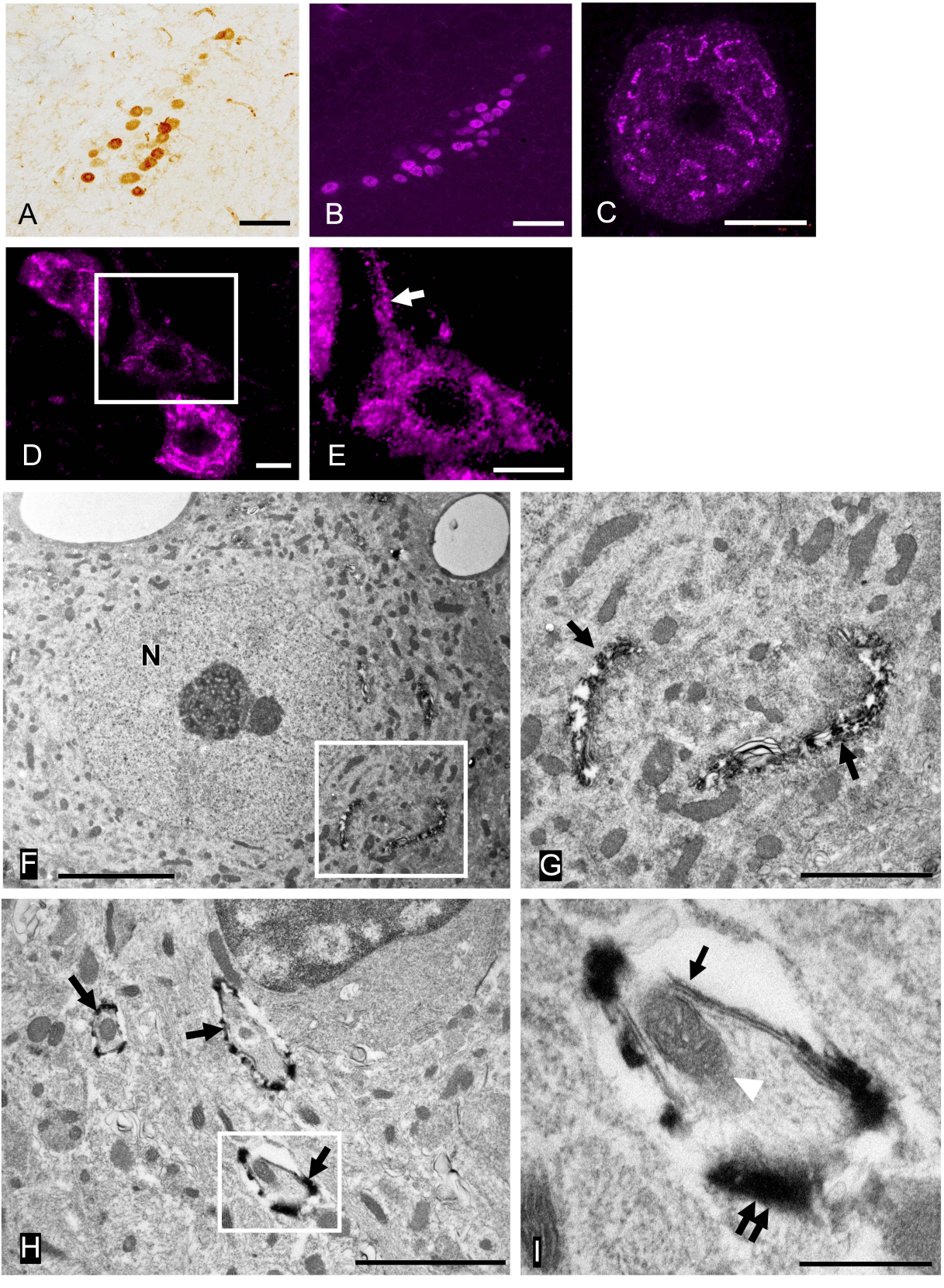
A
B
C
D
E
N
F
G
H
I

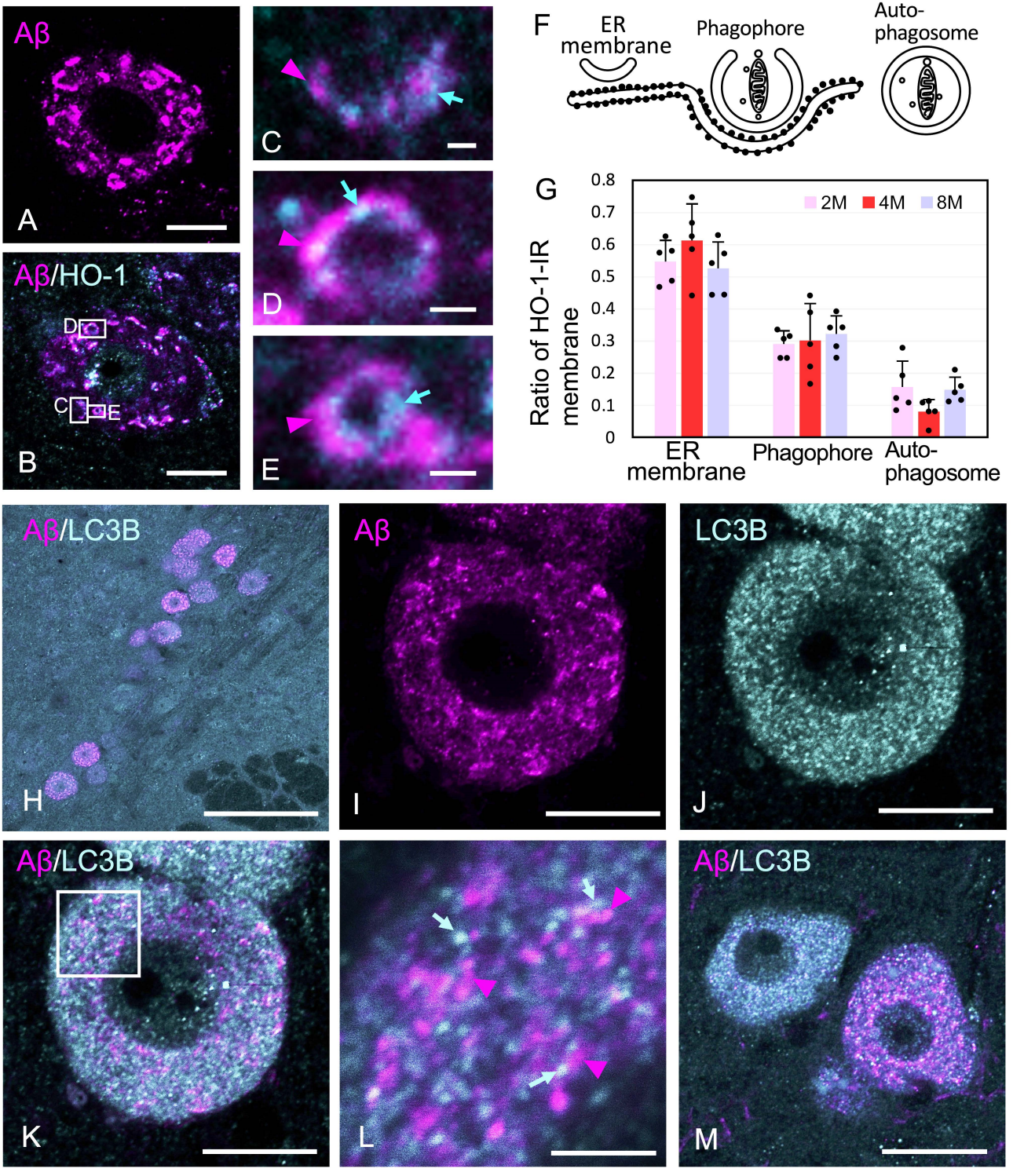
Aβ
A
C
D
E
Aβ/HO-1
D
C
E
B
F
ER membrane
Phagophore
Auto-phagosome
G
2M
4M
8M
Ratio of HO-1-IR membrane
0.8
0.7
0.6
0.5
0.4
0.3
0.2
0.1
0
ER membrane
Phagophore
Auto-phagosome
Aβ/LC3B
H
Aβ
I
LC3B
J
Aβ/LC3B
K
L
Aβ/LC3B
M

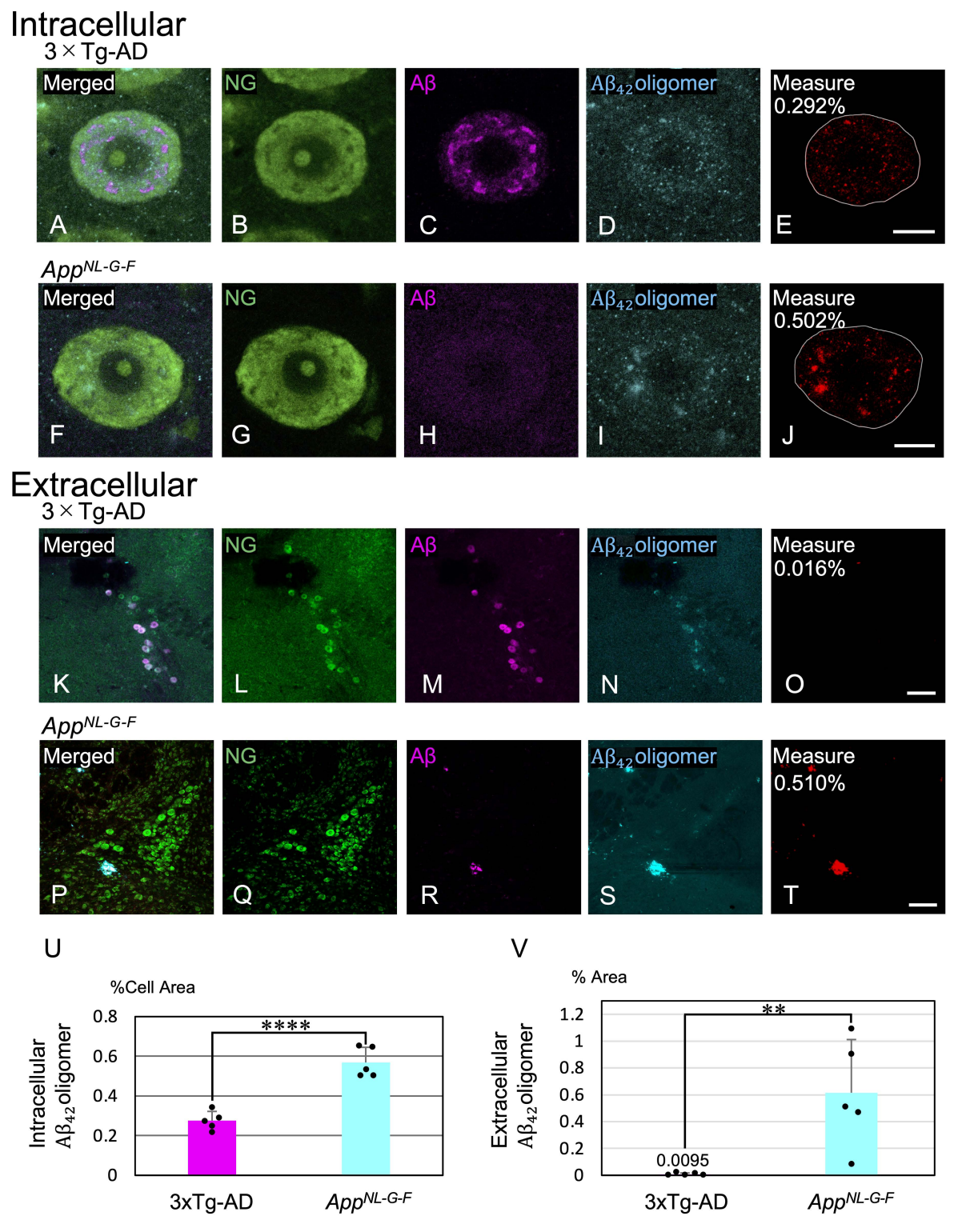
Intracellular
3 × Tg-AD
Merged
NG
Aβ
Aβ42oligomer
Measure
0.292%
A
B
C
D
E
App NL-G-F
Merged
NG
Aβ
Aβ42oligomer
Measure
0.502%
F
G
H
I
J
Extracellular
3 × Tg-AD
Merged
NG
Aβ
Aβ42oligomer
Measure
0.016%
K
L
M
N
O
App NL-G-F
Merged
NG
Aβ
Aβ42oligomer
Measure
0.510%
P
Q
R
S
T
U
%Cell Area
Intracellular Aβ42oligomer
0.8
0.6
0.4
0.2
0
****
3xTg-AD
App NL-G-F
V
% Area
Extracellular Aβ42oligomer
1.2
1
0.8
0.6
0.4
0.2
0
**
0.0095
3xTg-AD
App NL-G-F

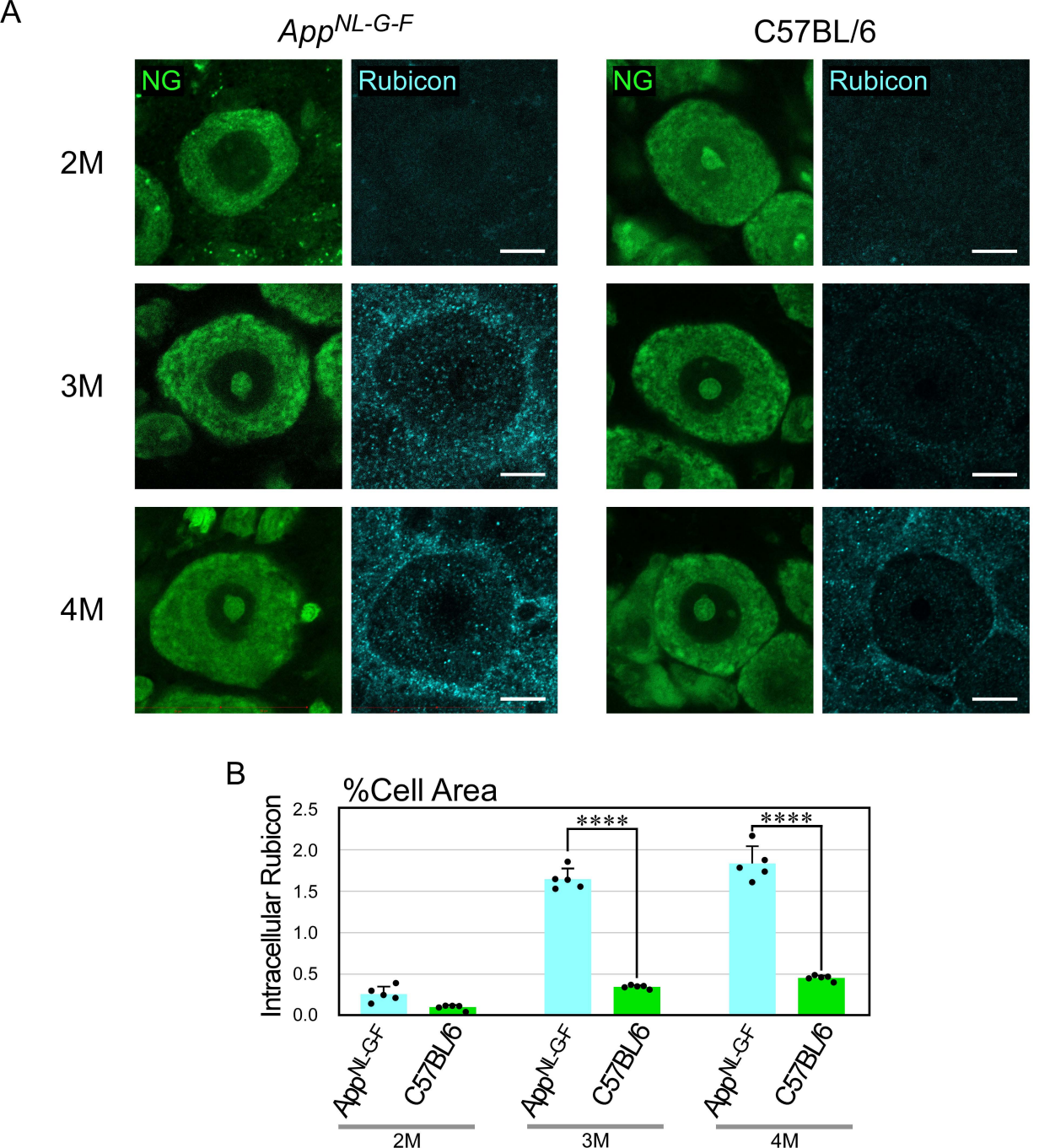
A
App^NL-G-F
C57BL/6
NG
Rubicon
NG
Rubicon
2M
3M
4M
B
%Cell Area
Intracellular Rubicon
2.5
2.0
1.5
1.0
0.5
0.0
****
****
App^NL-G-F
C57BL/6
App^NL-G-F
C57BL/6
App^NL-G-F
C57BL/6
2M
3M
4M

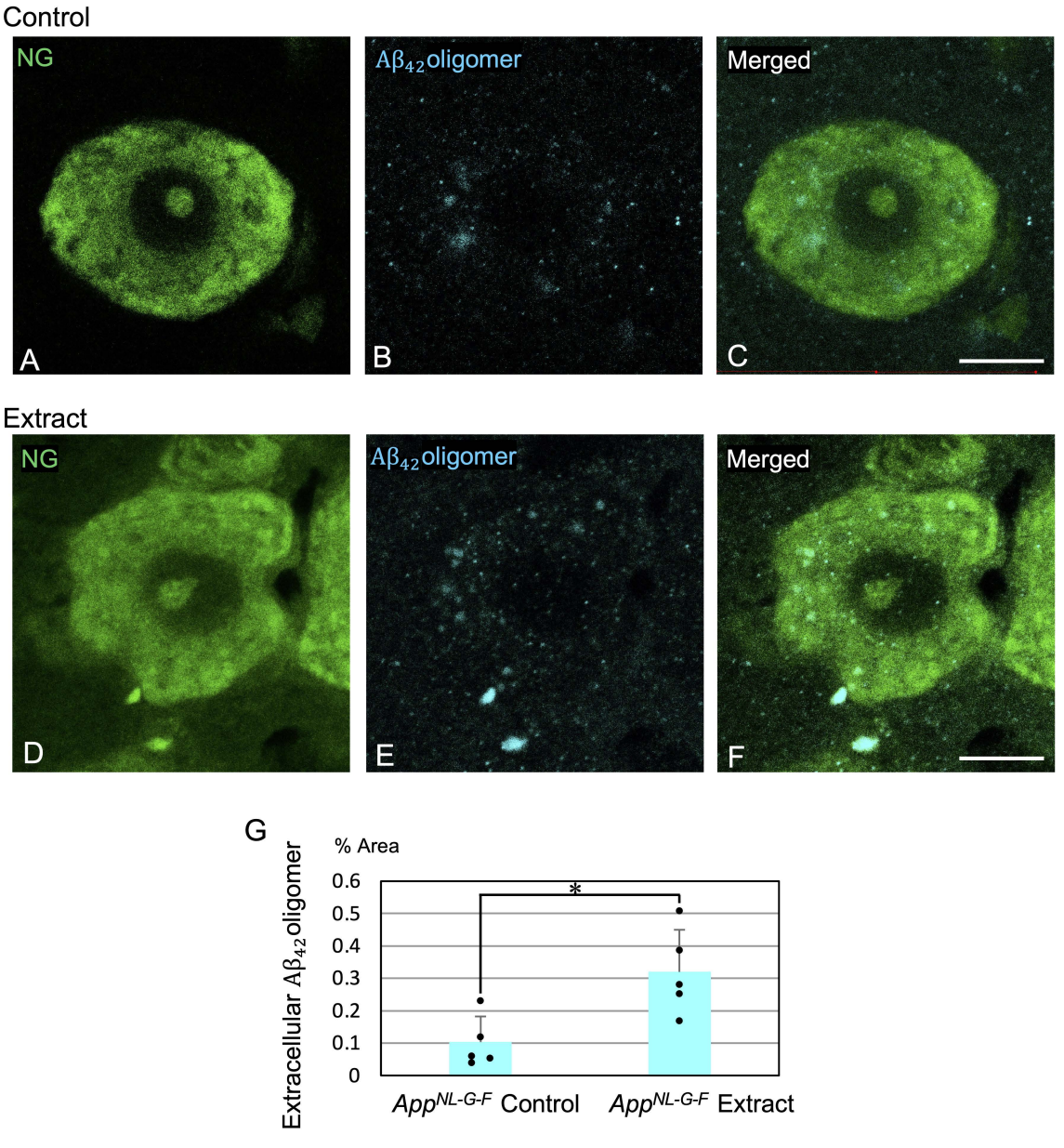
Control
NG
Aβ42oligomer
Merged
A
B
C
Extract
NG
Aβ42oligomer
Merged
D
E
F
G
Extracellular Aβ42oligomer
% Area
0.6
0.5
0.4
0.3
0.2
0.1
0
*
AppNL-G-F Control
AppNL-G-F Extract

Reduced Autophagy in Aged Trigeminal Neurons Causes Amyloid β Diffusion

R. Sonoda[1, 2], E. Kuramoto[2], S. Minami[1, 2], S-E. Matsumoto[3], Y. Ohyagi[4], T. Saito[5], T. Saido[6], K. Noguchi[1], and T. Goto[2]

[1]Department of Periodontology, Graduate School of Medical and Dental Sciences, Kagoshima University, Kagoshima, Japan.
[2]Department of Oral Anatomy and Cell Biology, Graduate School of Medical and Dental Sciences, Kagoshima University, Kagoshima, Japan.
[3]Department of Immunology, Graduate School of Medical and Dental Sciences, Kagoshima University, Kagoshima, Japan.
[4]Department of Neurology and Geriatric Medicine, Ehime University Graduate School of Medicine, Ehime, Japan.
[5]Department of Neurocognitive Science, Institute of Brain Science, Nagoya City University Graduate School of Medical Sciences, Nagoya, Japan.
[6]Laboratory for Proteolytic Neuroscience, RIKEN Center for Brain Science, Wako, Japan.

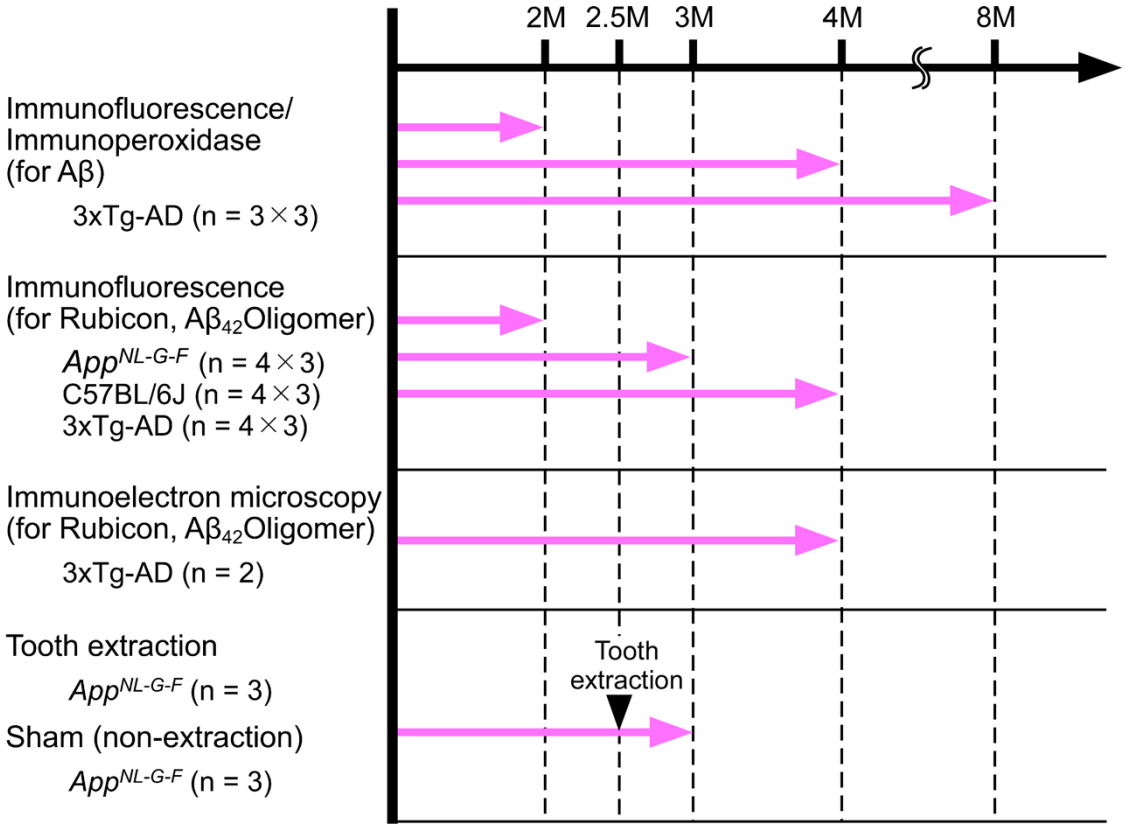

Appendix Figure 1. Experimental design. For Immunofluorescence/Immunoperoxidase, 3×Tg-AD mice were euthanized and fixed at 2, 4, 8 months after birth. For immunofluorescence (Rubicon and $A\beta_{42}$ oligomers), *App*$^{NL-G-F}$, C57BL/6, and 3×Tg-AD mice were euthanized and fixed at 2, 3, 4 months after birth. For immunoelectron microscopy, 4-month-old 3×Tg-AD mice were euthanized and fixed. For tooth extraction model, right molars of *App*$^{NL-G-F}$ mice were extracted at 2.5 months after birth.

Surgery

The molars were extracted as described previously (Goto et al., 2020). For tooth extraction, 2.5-month-old *App*$^{NL-G-F}$ mice (n = 6) were anesthetized using a combination of medetomidine (0.15 mg/kg; Kobayashi Kako), midazolam (2 mg/kg; Astellas Pharma), and butorphanol (2.5 mg/kg; Meiji Seika) (Kirihara et al., 2013). The right first, second, and third molars of the anesthetized mice were extracted using a dental probe, whereas the left molars were not extracted. For analgesia, the extraction sockets were covered with jelly containing 2% xylocaine. Sham mice were anesthetized in the same way but were not extracted the teeth. The mice were fed a nutritious powdered diet (Rodent LabDiet 5L37; Nutrition International) and reared for 2 weeks until fixation.

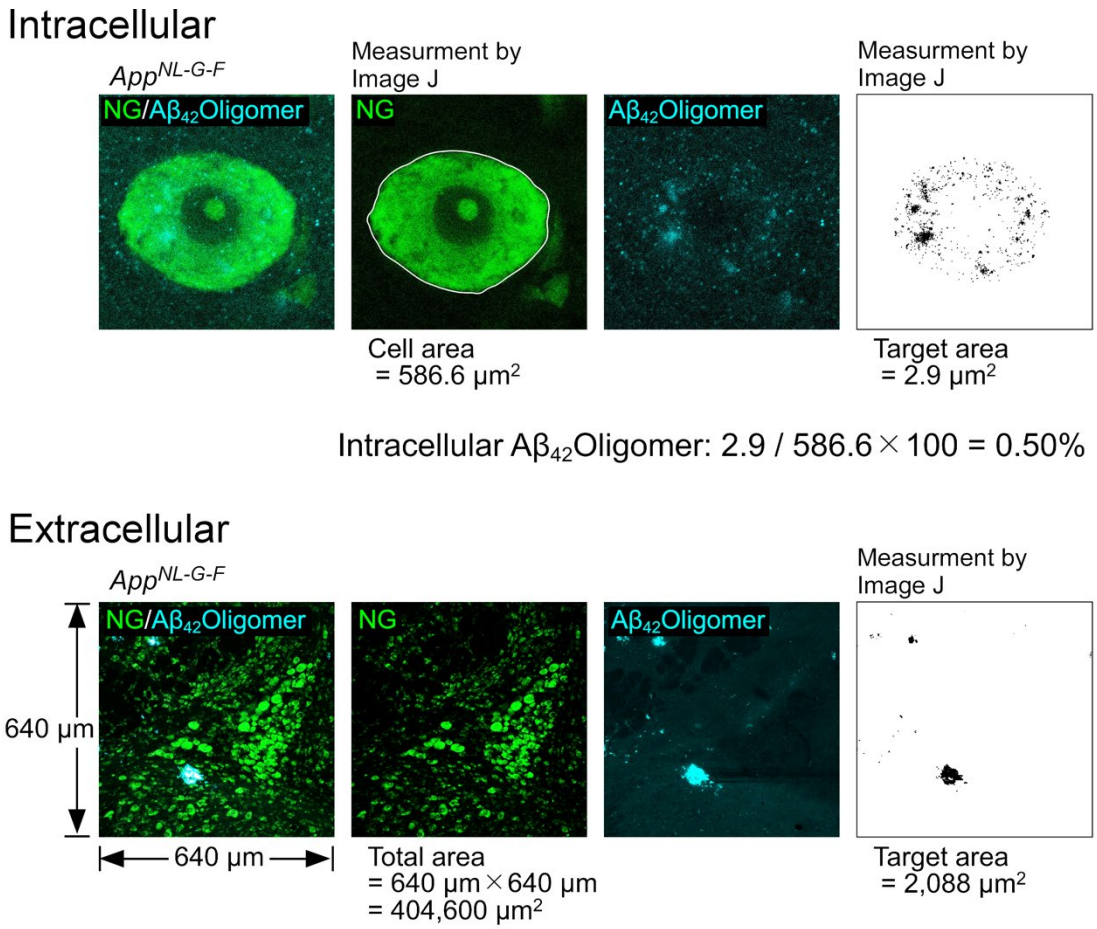

Appendix Figure 2. Intracellular Aβ42 oligomer and extracellular Aβ42 oligomer analysis methods. The area of cells was obtained by tracing the outline of Vmes neurons stained with NeuroTrace Green (NG) and measuring the area within the outline. Next, Aβ42 oligomer-immunopositive areas were extracted using ImageJ and their areas were measured. Intracellular Aβ42 oligomer was defined as target area/cell area × 100.
Extracellular Aβ42 oligomers were measured as follows: the Vmes were placed in the center of the image, and the Aβ42 oligomer immunopositive region in a 640 μm × 640 μm area (total area) excluding the Vmes region was extracted, and that region was defined as the target area. Extracellular Aβ42 oligomers were defined as target area/total area × 100.

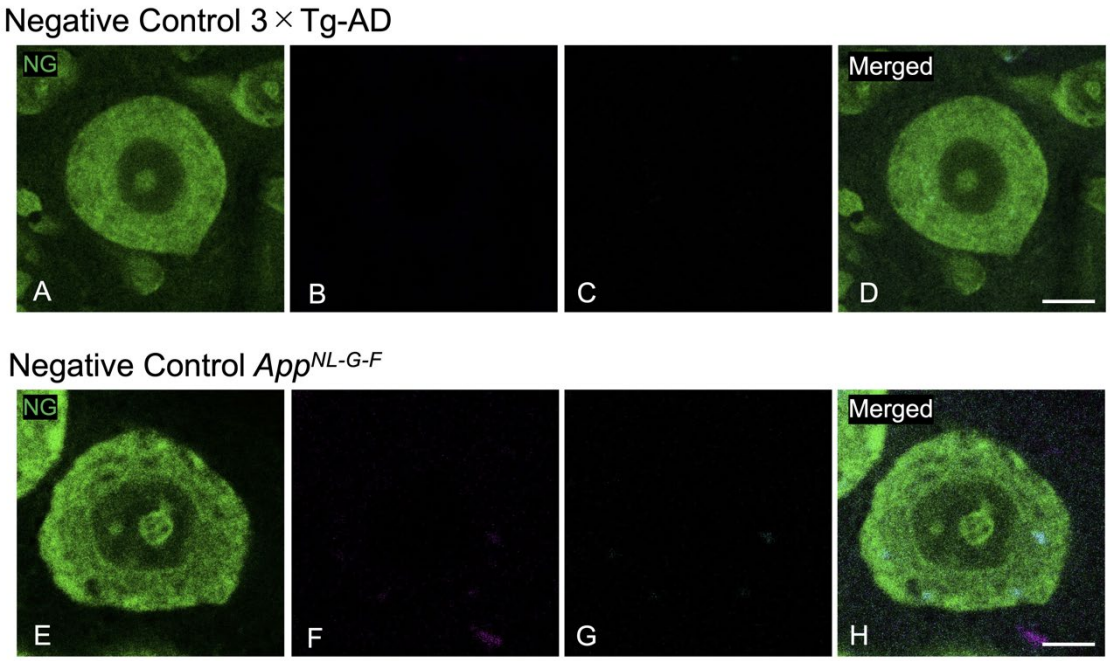

Appendix Figure 3. Negative control for immunofluorescence staining. The sections were immunostained with the primary antibodies, except for those against Aβ (mouse anti-β-amyloid (1–16) antibody;1:1,000; 6E10; BioLegend) (**B, F**) and $A\beta_{42}$ oligomers (rabbit anti-β Amyloid (1-42)-Conformation Specific; 1:1,000; GeneTex) (**C, G**). Donkey anti-mouse IgG H&L (Alexa Fluor 555; excitation, 543 nm; emission, 590–625 nm) and donkey anti-rabbit IgG H&L (Alexa Fluor 647; excitation, 633 nm; emission, ≥ 650 nm) were used as secondary antibodies. The sections were counterstained with NeuroTrace Green (NG; excitation 488 nm, emission 505–530 nm). Digital images were captured under the confocal laser-scanning microscope (LSM 900; Zeiss), with an oil immersion 63× objective (Plan-Apochromat, numerical aperture = 1.4; Zeiss) and a pinhole 1.0 Airy unit. (**A**–**D**) Negative control for 3×Tg-AD mice. (**E**–**H**) Negative control for *App*$^{NL-G-F}$ mice. Scale bar = 10 μm.

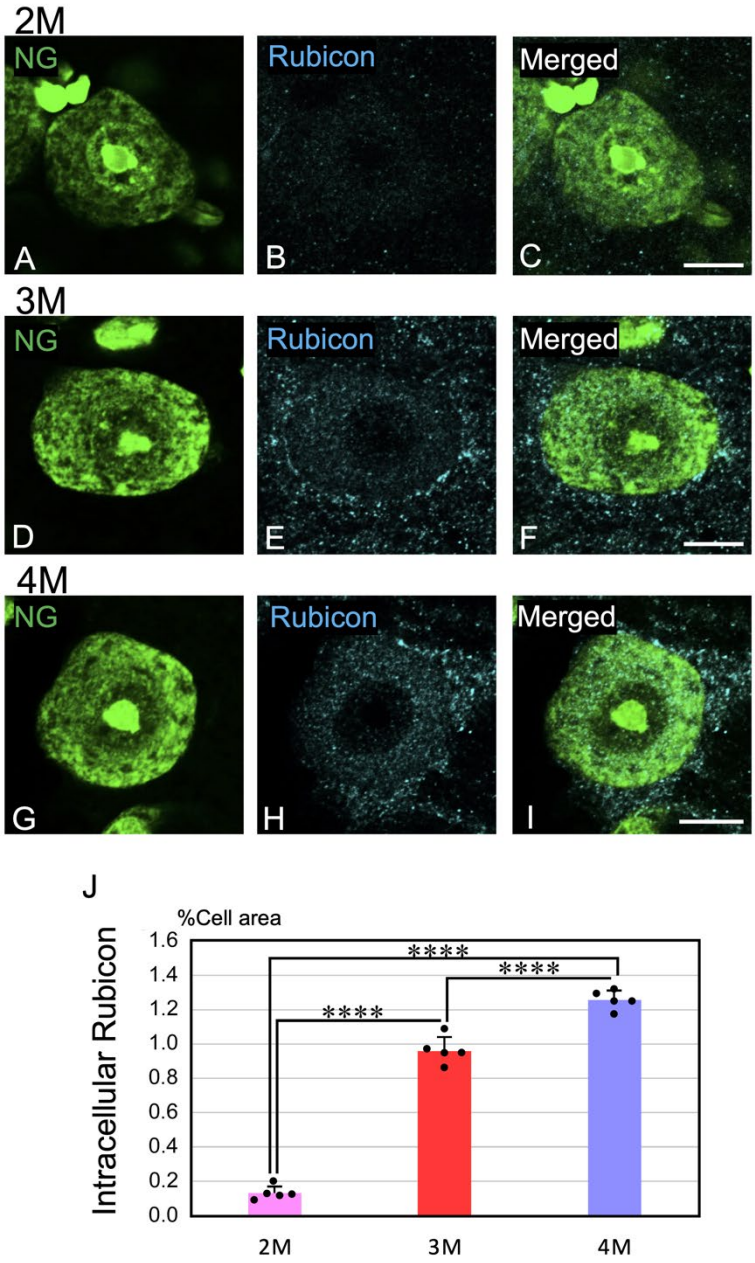

Appendix Figure 4. Increased Rubicon expression in aged Vmes neurons from 3×Tg-AD mice. (**A**–**I**) Vmes neurons from 3×Tg-AD mice aged 2–4 months were stained for Rubicon (Alexa Fluor 647; excitation, 633 nm; emission, ≥ 650 nm). (**A**, **D**, **G**) The sections were counterstained with NeuroTrace Green (NG; excitation 488 nm, emission 505–530 nm). For quantitative analysis (G), we selected 15 sections, which were spaced at regular intervals within the caudal half part of the Vmes from 12 3×Tg-AD mice. We captured images of a randomly selected one Vmes neuron per section using the confocal laser-scanning microscope (LSM 900; Zeiss) with an oil immersion 63× objective (Plan-Apochromat , numerical aperture = 1.4; Zeiss) and a pinhole 1.0 Airy unit. (**J**) Graph

showing the difference in the ratio of Rubicon positivity to the cell area, as shown in Figure 3. A–I. Scale bar = 10 μm. Data are means ± SDs, n = 5. ****p < 0.0001, one-way analysis of variance followed by Tukey's post hoc test.

References

Kirihara Y, Takechi M, Kurosaki K, Kobayashi Y, Kurosawa T. 2013. Anesthetic effects of a mixture of medetomidine, midazolam and butorphanol in two strains of mice. Exp Anim. 62(3):173-180.

Goto T, Kuramoto E, Dhar A, Wang RP, Seki H, Iwai H, Yamanaka A, Matsumoto SE, Hara H, Michikawa M, Ohyagi Y, Leung WK, Chang RC. 2020. Neurodegeneration of trigeminal mesencephalic neurons by the tooth loss triggers the progression of Alzheimer's disease in 3×Tg-AD model mice. J Alzheimers Dis. 76(4):1443-1459.